OBLIQUE INTERNAL TIDE GENERATION

A THESIS SUBMITTED TO THE GRADUATE DIVISION OF THE
UNIVERSITY OF HAWAI‘I AT MĀNOA IN PARTIAL FULFILLMENT
OF THE REQUIREMENTS FOR THE DEGREE OF

MASTER OF SCIENCE

IN

OCEANOGRAPHY

DECEMBER 2014

By

Adam P. Jenkins

Thesis Committee:

Glenn Carter, Chairperson
Janet Becker
Doug Luther
Mark Merrifield

We certify that we have read this thesis and that, in our opinion, it is satisfactory in scope and quality as a thesis for the degree of Master of Science in Oceanography.

THESIS COMMITTEE

_____
Chairperson

_____

_____

_____

To my wonderful wife,

Kristina Noelani Jenkins

Acknowledgments

I want to thank my committee for their wisdom and advice. I want to thank my chairperson for his support and mentorship. I want to thank my wife for always believing in me.

Abstract

An important pathway for the dissipation of barotropic tidal energy in the ocean results from the generation of baroclinic tides at seamounts and ridges. A nonlinear hydrostatic model is used to study how barotropic to baroclinic energy conversion is affected by the Coriolis force and the orientation of undersea ridges with respect to the tidal propagation direction.

Results show nearly symmetric lobes of depth-integrated baroclinic energy flux on both sides of a ridge oriented normal to the tidal velocity when the Coriolis parameter is zero and the model is forced with a rectilinear tide. This energy flux is distributed between narrow beams that emanate upward from the ridge top and much wider structures fanning downward and outward from the ridge. Rotating the ridge with respect to the tidal direction distorts the shape of the beams and reduces the overall energy flux gradually at first, then much more rapidly as the relative incidence angle (RIA) approaches zero. The energy flux is a simple function of the RIA and the aspect ratio of the ridge, which follows from the assumption that the energy flux is proportional to the maximum slope of the ridge and the effective area the ridge presents to the oncoming tide.

When the model is forced by elliptical tidal currents, the directivity of the resulting internal tide beams is reduced but the energy flux is increased relative to the case of rectilinear tidal forcing for the same tidal current magnitude. The resulting energy flux is the sum of the effects of treating the tidal ellipse as two rectilinear tides along the principal axes, 90° out of phase.

Table of Contents

List of Figures

Chapter 1

Introduction

Internal tides (internal waves at tidal frequencies) are omnipresent in the stratified ocean (e.g., Rainville and Pinkel, 2006; Dushaw, 2006; Egbert and Ray, 2000) and may be generated by the raising and lowering of isopycnals by the surface tidal flow over seamounts and undersea ridges. Internal energy radiates away from a source in a direction with vertical and horizontal components along characteristics (defined below). In an ocean with constant stratification, the characteristics will be straight lines whose slope is determined from the dispersion relation for internal waves after making simplifying assumptions, such as the Boussinesq and small amplitude approximations. A unique feature of internal waves is that their phase propagates along the wavenumber direction at a right angle in the vertical plane to their energy.

The theory for the conversion of the barotropic (surface) tide to baroclinic (internal) tidal energy was set forth in the studies of Baines (1973), Bell (1975a), and Bell (1975b). Baines' approach of using characteristics could, in principle, be applied to the baroclinic generation problem at both subcritical topography (features with slopes less than the slope of the internal wave rays) and supercritical topography (features with maximum slopes greater than the slope of internal wave rays). Bell developed a method that applied to bottom topography "flat" enough that the bottom boundary condition could be applied at $z = 0$ rather than the actual seafloor at $z = -H + h(x, y)$. While this restricts its applicability, this method has value because of its validity for finite excursion parameters ku_0/ω. This dimensionless parameter is a ratio of the tidal excursion distance u_0/ω to the horizontal length scale $1/k$ of the topography, where u_0 is the magnitude of the barotropic tidal

current, and ω is the angular frequency. For sinusoidal topography, k is the horizontal wavenumber. This tidal excursion parameter is one of four that characterize the internal tide generation problem (Garrett and Kunze, 2007). Another important parameter is the ratio of a measure of the topographic slope to the characteristic slope, given by $\epsilon = kH_0/s_{char}$, where H_0 is the topographic height and

$$s_{char} = \sqrt{\frac{\omega^2 - f^2}{N^2 - \omega^2}} \tag{1.0.1}$$

is the slope of small-amplitude characteristics propagating with angular frequency ω through a medium with buoyancy frequency N and Coriolis parameter f. There are other slightly different definitions of the parameter ϵ, such as the ratio of the onshore or maximum topographic slope to the characteristic slope (Hall and Carter, 2010; Balmforth and Peacock, 2009):

$$\epsilon = \sqrt{\frac{N^2 - \omega^2}{\omega^2 - f^2}} \left| \frac{dh}{dx} \right|_{max}. \tag{1.0.2}$$

The other two important non-dimensional parameters ω/N and ω/f describe the proximity of the wave frequency to the limits for oscillating waves, N and f.

More recent studies of internal tide generation are generally divided between analytical studies with idealized topography (e.g., Munroe and Lamb, 2005; Llewellyn Smith and Young, 2003; St. Laurent et al., 2003) and numerical studies focusing on key generation sites in the real ocean (e.g., Carter et al., 2008; Simmons et al., 2004; Niwa and Hibiya, 2001). St. Laurent et al. (2003) examined knife-edge and other ridges in a finite depth ocean using modal expansions for different values of $\delta = H_0/H$, where H_0 is the ridge height and H the full ocean depth. They found that when $\delta \ll \epsilon$, a vertical knife-edge ridge generated twice the energy of a critical "Witch of Agnesi" barrier of the same height, whose shape is given by

$$h = \frac{H_0}{1 + \mu^2 x^2}, \tag{1.0.3}$$

with μ chosen so that $s_{topo} = s_{char}$. This suggests that the height of a supercritical deep ocean ridge is more important than the ridge slope in determining the energy flux generated. Llewellyn Smith

and Young (2003) used a different analytical solution to show that the knife-edge barrier vs. "Witch of Agnesi" barrier result holds as long as $\delta \ll 1$.

Holloway and Merrifield (1999) conducted a numerical study on idealized three-dimensional Gaussian-shaped seamounts and undersea ridges with a rectilinear surface tide directed normal to the ridge. They found that elongated ridges were more effective than symmetric seamounts of the same slope at converting barotropic energy to baroclinic energy. As Garrett and Kunze (2007) summarized, "large seamounts are ineffective at generating internal tides unless they are elongated in a direction normal to the barotropic current," because broad ridges nearly perpendicular to flow tend to block the barotropic current from bypassing the ridge. In a later numerical study of realistic bathymetry along the Hawaiian Ridge, Merrifield and Holloway (2002) showed that baroclinic energy flux was strongest at sites of enhanced barotropic forcing, suggesting that barotropic flow over features is a significant factor in the generation of baroclinic energy along the Hawaiian Ridge as well as the criticality of the slope. Carter et al. (2008) investigated the energy budget in numerical simulations in a subregion of the Hawaiian Ridge and showed that 84% of the energy lost from the barotropic tide was converted to internal tides at key generation sites near the islands of O'ahu and Kaua'i such as the steep-sided Ka'ena Ridge.

To date, idealized three-dimensional numerical studies have focused on orientations of tide and topography expected to yield the highest conversion rate (e.g., Holloway and Merrifield, 1999; Munroe and Lamb, 2005). Although three-dimensional studies have been done on internal wave reflection (Eriksen, 1982), to our knowledge, no idealized numerical studies have examined conversion by a surface tide impinging obliquely on a supercritical submarine ridge. This study seeks to fill this gap. Chapter 2 discusses the methods used to numerically model baroclinic generation by topography and to analyze the model output using the example of a non-rotating tide propagating perpendicular to the long axis of a ridge. Chapter 3 discusses the results of model runs that vary the rectilinear tide's angle to the ridge. Chapter 4 extends the results to a rotating, elliptical tide. Chapter 5 summarizes the results.

Chapter 2

Methods

2.1 Princeton Ocean Model

The Princeton Ocean Model (POM) (Blumberg and Mellor, 1987) is a nonlinear, hydrostatic, free-surface, sigma-coordinate model with a Mellor and Yamada (1982)turbulence closure scheme. A mode-splitting technique separately calculates the fast-moving barotropic motions and slow-moving baroclinic motions, allowing the Courant-Friedrichs-Lewy (CFL) stability condition for the surface mode to be met while reducing the computational load by updating the internal mode at a time step 40 times longer than the external mode. The use of a terrain-following sigma-coordinate simulates barotropic flow near the bottom topography more accurately than a z-level grid; however, it creates an error in the pressure gradient over steep topography (e.g., Haney, 1991; Mellor et al., 1994; Ezer and Mellor, 1997). Mellor et al. (1994) found that the pressure gradient error is not numerically divergent with time and that it decreases with the square of the spatial grid cell dimensions. In addition, the harmonic analysis performed on the model results separates the energy flux at the M_2 constituent from the mean and linear growth terms, where the pressure gradient error may be expected to appear.

This study examines the effects of varying the relative incidence angle (RIA) between the barotropic tide and the major axis of the ridge. This is the angle between the long axis of a ridge and the wave vector of the surface tide propagating over the ridge. Here, the ridge is a Gaussian

seamount whose elevation z is given by

$$z = -H + H_0 \cdot exp\left(-\frac{x^2}{A^2} - \frac{y^2}{B^2}\right), \tag{2.1.1}$$

where $z = 0$ is the surface, $H_0 = 2.5$ km is the ridge-height, and $H = 5$ km is the open ocean water column height. The minor and major ridge length scales are $A = 23$ km and $B = 69$ km, respectively, giving the ridge an aspect ratio B/A of 3:1. A constant stratification of $N = 4 \times 10^{-3} \frac{rad}{s}$ is used throughout this study. The model domain is 400 km x 400 km with a horizontal resolution of 2 km and 200 sigma layers in the vertical direction. A 10-cell wide relaxation layer was used to prevent baroclinic energy from reflecting off the boundaries.

The model was forced using the Flather open boundary condition (Flather, 1976; Carter and Merrifield, 2007) with a single sinusoid at the M_2 frequency having an amplitude of $\eta = 0.5$ m. To vary the RIA, the tidal propagation direction remains fixed towards the northeast while the ridge is rotated in increments of 11.25°. This approach is necessary since the tide must propagate at a non-zero angle to at least two boundaries to make use of the Flather open boundary condition, since the Flather condition applied with a zero angle does not converge to the result for a channel. With no Coriolis force ($f = 0$), the Flather condition adjusts the elevation and normal velocity at an open boundary to externally prescribed values (Carter and Merrifield, 2007) that represent the incoming surface tide as free shallow-water gravity wave with an elevation η and horizontal velocities u and v given by:

$$\eta = \eta_0 \cos\left(kx + ly - \omega t + \phi_\eta\right), \tag{2.1.2}$$

$$u = \sqrt{\frac{g}{H_0}} \frac{k}{\kappa} \eta_0 \cos\left(kx + ly - \omega t + \phi_\eta\right), \quad \text{and} \tag{2.1.3}$$

$$v = \sqrt{\frac{g}{H_0}} \frac{k}{\kappa} \eta_0 \cos\left(kx + ly - \omega t + \phi_\eta\right), \tag{2.1.4}$$

where k and l are the zonal and meridional components of the wavenumber vector $\vec{\kappa}$, ω is the M_2 frequency, and ϕ_η is the initial phase of the elevation. In addition to affecting the physics in the domain interior, the introduction of rotation ($f \neq 0$) requires elliptical boundary forcing of the

surface tide. This tide enters the boundaries as a free shallow-water rotating gravity wave, aka a Poincaré wave after the usage in Gill (1982), given by:

$$\eta = \eta_0 \cos(kx + ly - \omega t + \phi_\eta), \tag{2.1.5}$$

$$u = \frac{\sqrt{f^2 + gH_0k^2}}{H_0\kappa}\eta_0 \cos(kx + ly - \omega t + \phi_\eta + \phi_a), \quad \text{and} \tag{2.1.6}$$

$$v = \frac{\sqrt{f^2 + gH_0l^2}}{H_0\kappa}\eta_0 \cos(kx + ly - \omega t + \phi_\eta - \phi_b), \tag{2.1.7}$$

where $\phi_\eta + \phi_a$ and $\phi_\eta - \phi_b$ are the initial phases of the zonal and meridional velocities. The velocity phase offsets are given by

$$\tan\phi_a = \frac{fl}{\omega k} \quad \text{and} \tag{2.1.8}$$

$$\tan\phi_b = \frac{fk}{\omega l} \tag{2.1.9}$$

and the frequencies and wavenumber are linked via the dispersion relation

$$\omega^2 = f^2 + gH_0\kappa^2. \tag{2.1.10}$$

Most model runs lasted for 18 M_2 tidal cycles. The forcing is ramped up gradually over the first four tidal cycles and a harmonic analysis is performed after ten tidal cycles to isolate the M_2 frequency using a singular value decomposition technique, producing elevation, horizontal barotropic (depth-averaged) velocities and total horizontal and vertical velocities. Baroclinic velocities are obtained by subtracting the depth-averaged velocities from the total velocities.

2.2 Energy Flux

The baroclinic energy flux is calculated following Gill (1982):

$$F = \langle p'u' \rangle, \tag{2.2.1}$$

where u' is the M_2 baroclinic velocity perturbation and p' is the pressure perturbation. The pressure perturbation is calculated following Kunze et al. (2002):

$$p'(z) = -\int_z^0 N^2\,\xi(z')\,dz' - \frac{1}{H}\int_{-H}^0\int_z^0 N^2\,\xi(z')\,dz'dz, \tag{2.2.2}$$

where integrating the harmonic vertical velocity $w = -i\omega\xi$ gives the vertical displacement ξ. To illustrate the method, consider a rectilinear tide whose wavenumber vector is perpendicular to the major axis of the ridge (i.e. the RIA $= 90°$). In this case (hereafter called RT90), the barotropic tide generates baroclinic energy flux that radiates away in a beam perpendicular to the ridge. In the vertical direction, energy radiates upwards and downwards following the characteristic slope from a near-critical region just below the ridge crest (Fig. 2.1). In order to compare the intensity and distribution of the radiated energy flux as a function of RIA, the normal component of the baroclinic energy flux that propagates out of a cylindrical control volume was calculated. A cylinder radius of 100 km (vertical lines on Fig. 2.1) is used as it contains the region of energy conversion, while excluding the crossing of the initially upward and downward propagating beams after they reflect off the surface and seafloor. Between the ridge and the crossing site, the energy in the upper and lower portions of the water column is dominated by the energy of these upward and downward beams, respectively.

The energy in a volume of the water column can be calculated from the energy flux by two different methods, related by the divergence theorem. This theorem may be applied to an arbitrary shape; a right circular cylinder centered on the ridge was chosen for convenience. The divergence theorem relates sources and sinks of energy flux within the cylinder to the flux passing through the boundaries of that cylinder. More formally,

$$\iint_S \vec{E}\cdot\mathrm{d}\vec{A} = \iiint_V \nabla\cdot\vec{E}\,\mathrm{d}V, \tag{2.2.3}$$

where V represents the volume of the cylinder, $\vec{E}$ is the baroclinic energy flux, and S represents the surface of the cylinder, including the top and bottom. The volume integral of the flux divergence

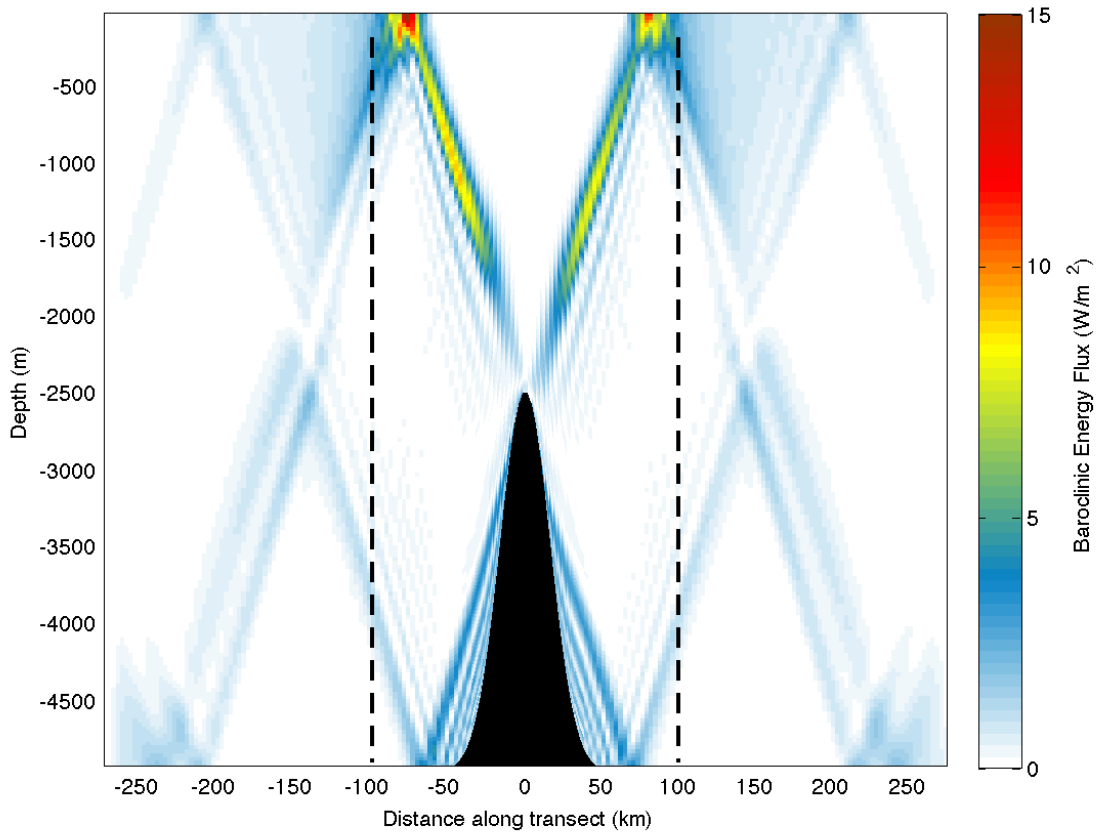

Figure 2.1. Baroclinic energy flux for the RT90 case along a vertical cross-section parallel to the tide. Beams of energy radiate away from the critical slopes near the ridge crest while a more complex structure is created at the ridge flanks. The ridge has a 3:1 aspect ratio and the tide propagates perpendicular to the ridge's semi-major axis.

represents the net gain or loss of baroclinic energy within the cylinder. Positive divergence is a source of energy while negative divergence is a sink. The surface integral of the normal component of baroclinic energy flux represents the net gain or loss of baroclinic energy that passes through the boundaries of the cylinder. By definition, positive flux is out of the cylinder.

Here, we are focused on the different behavior of the upward and downward baroclinic energy radiating away through the vertical walls of the cylinder. Equation 2.2.3, therefore, may be rewritten as

$$\iint\limits_{S_{wall}} \vec{E} \cdot \mathrm{d}\vec{A} = \iiint\limits_{V} \nabla \cdot \vec{E}\, \mathrm{d}V - \iint\limits_{S_{top}} \vec{E} \cdot \mathrm{d}\vec{A} - \iint\limits_{S_{bottom}} \vec{E} \cdot \mathrm{d}\vec{A}. \tag{2.2.4}$$

The right-hand side is dominated by the flux through the bottom, while the other two terms are negligible. Since the left-hand side, $\iint\limits_{S_{wall}} \vec{E} \cdot \mathrm{d}\vec{A}$, is a direct calculation of the desired quantity, the following discretized version of it will be used throughout this study:

$$\text{Radiated Energy Flux} = \sum\sum \vec{E} \cdot \vec{\mathrm{n}}\, \Delta h\, \Delta\theta, \tag{2.2.5}$$

where the energy flux normal to the cylinder wall $\vec{E} \cdot \vec{\mathrm{n}}$ is summed over the depth (h) and the azimuthal direction (θ). The depth may run from the seafloor to the ridge top to encompass the downward-propagating energy, or from the ridge top to the sea surface to encompass the upward-propagating energy; the sum of these gives the total energy flux radiating away from the ridge. Not only is the left-hand side of Equation. 2.2.4 a more direct calculation, but this term is simpler to evaluate than calculating $\iint\limits_{S_{bottom}} \vec{E} \cdot \mathrm{d}\vec{A}$, which appears to introduce a horizontal resolution independent error of 5–10%.

Estimates of conversion are given by Carter et al. (2008) in their equations (4) and (5) and their appendix. After expressing the energy equation in a sigma-coordinate system, a barotropic energy equation is obtained by vertically averaging the total energy equation. The baroclinic energy balance is defined as the total energy minus the barotropic components. Terms involving tendency (time-varying energies), flux divergence, advection, and dissipation are identified in both the barotropic and baroclinic energy equations; the remaining terms represent the conversion: a loss

in the barotropic energy equation produces a gain in the baroclinic. Although they are calculated differently, the magnitudes of these two methods of computing the conversion agree to within 10% in their model of the Hawaiian Ridge (Carter et al., 2008).

The radiated energy (Eqn. 2.2.5) for the RT90 case if presented as a function of radial distance from the center of the ridge (Fig. 2.2). The outward normal flux agree within 5% of the conversion of barotropic to baroclinic energy calculated within the model using the method described in Carter et al. (2008). That study achieved similar results between different estimates of the conversion in a study of internal tide generation at the Kaena Ridge. The energy flux from the harmonic analysis is interpolated at equally spaced intervals along the angular, radial and vertical directions when viewed in a cylindrical coordinate system. This simplifies the calculation of area and volume elements when determining the surface integral of normal flux or the volume integral of flux divergence in the discrete analog to the divergence theorem. Interpolating this system of points at a finer resolution improves the accuracy until the resolution of the model output is reached. Increasing the spatial and temporal resolution of model runs improves the results further, particularly in the vicinity of the knee of the curve at 70 km where the surface and bottom bounces are occurring.

To highlight the differences between the upward and downward energy radiating from the ridge, the outward normal flux also is calculated for cylinders in the upper and lower halves of the water column. Here, the ridge top is set at a depth of 2500 meters. The upper cylinder (red line in Fig. 2.2) extends from this depth up to the sea surface, while the lower cylinder (blue line) extends from 2500 m down to the sea floor. As long as the radius of the cylinder is such that the upward and downward beams have not yet crossed, then the upward and downward beams are still contained in the upper and lower cylinders, respectively. For the stratification used, $N = 4 \times 10^{-3} \frac{\mathrm{rad}}{\mathrm{s}}$, these beams cross at about 130 km from the ridge (Fig. 2.1).

One method of estimating the conversion at a source of baroclinic energy flux is to determine the energy flux out the sides of a control volume, although the total radiated energy flux will be reduced with increasing distance from the ridge due to dissipation in the water column. The benefit of this approach is that the energy analysis does not need to be performed while the model is running, enabling faster model runs; however, it is likely to be less accurate because of the 5-10%

error mentioned above, although the energy analysis code calculates the conversion via two different methods which do not always agree.

2.3 Tide Perpendicular to a Ridge

The upward-radiating energy flux is concentrated in a narrower beam than the beam radiating toward the seafloor. Figure 2.3 shows a series of horizontal cross-sections of baroclinic energy flux for the RT90 model run. Below the top of the ridge, wide arcs of energy radiate downward and outward on both sides of the ridge, eventually reflecting off the seafloor. Two narrower arcs of energy radiate upward from the source near the ridge top, converging into intense narrow beams above the ridge that reflect off the surface. The crossing of the upward and downward beams is seen in the slice at 2500 m as an arc about halfway between the ridge and the edge of the domain.

The compactness of the upward beam is likely to be a more general result for simple ridge shapes like this. A simple explanation for this concentration of energy in the upper beams is possible if the beams radiate parallel or anti-parallel to the local gradient direction in the critical areas of the slope. In this case, upward propagating ray paths will tend to converge, while downward propagating characteristics will tend to diverge. This upward convergence is illustrated in Figure 2.4. The opposite should hold true for a valley in the seafloor with this same shape.

2.4 Depth-Integrated Energy Flux vs. Azimuthal Angle

Figure 2.5 shows the depth-integrated outward normal energy flux as a function of azimuthal angle for a RIA of 90° between the tide and the ridge's semi-major axis. This orientation, the perpendicular case of a tide normal to a ridge, is the most efficient generator of baroclinic energy. The surface tide propagates toward the northeast and is represented by the magenta arrow. The radial dimension is the depth-integrated energy flux, averaged over a tidal cycle, in units of Watts per meter. Ridge contours are superimposed to show the relative orientation of the ridge, surface tide, and baroclinic energy patterns. The blue line is the depth-integrated energy flux in the lower half of the water column, at a distance of 100 km from the ridge center, while the red line represents the

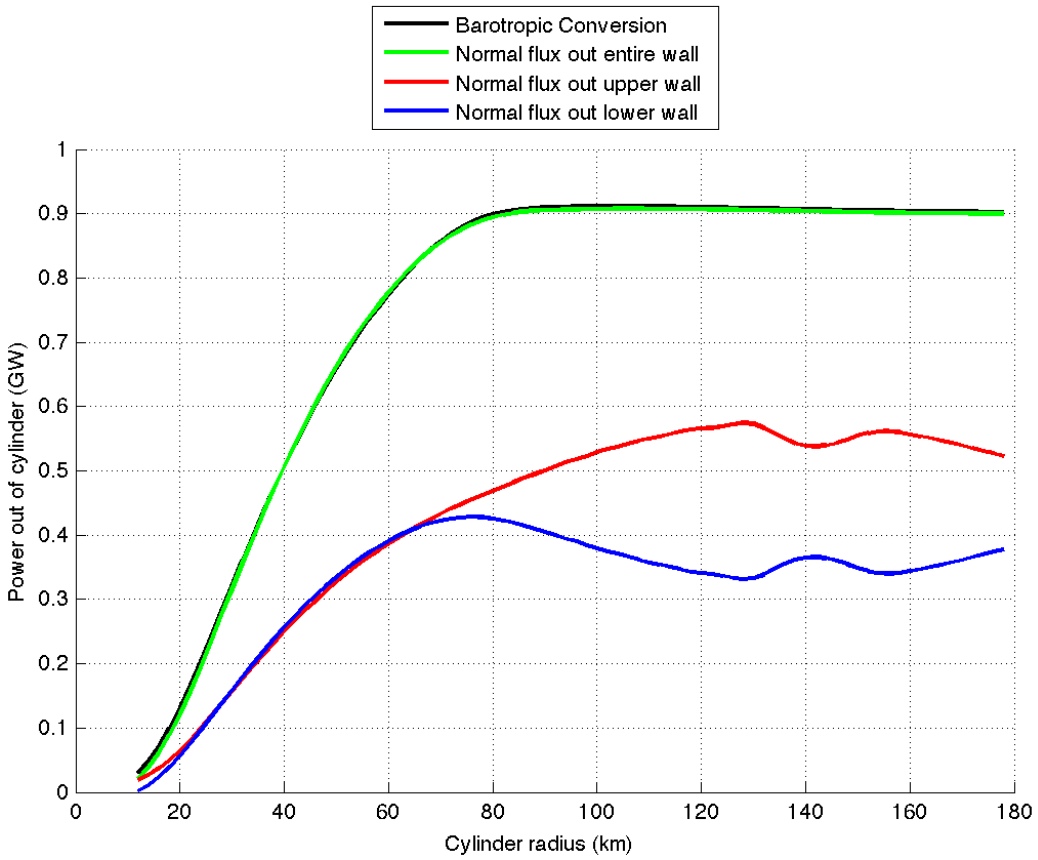

Figure 2.2. Baroclinic conversion and normal energy flux radiating out of a cylinder are shown as a function of radius. The black curve is the conversion of barotropic energy to baroclinic, calculated within the model. The green curve shows the total normal energy flux out of the walls of a circular cylinder. The red and blue curves are the normal energy flux out of the sides of the upper and lower halves of the water column, respectively, a rough representation of upward-propagating energy and downward-propagating energy. The knee of the black and green curves coincides with the bottom bounce of the downward beam at about 70 km from the ridge and the surface bounce of the upward beam at about 80 km from the ridge. A cylinder of radius 100 km or larger effectively encompasses the entire generation area, and the outward energy flux at this distance is insensitive to the model resolution. The gradual reduction in the total radiated energy flux beyond 100 km is due to the mild dissipation in the model.

upper half of the water column. At 100 km, the upper and lower beams leaving the ridge just below the crest have not yet crossed , so this division separates the beams initially leaving the ridge on an upward trajectory from those on a downward trajectory. The green line represents the energy flux depth-integrated over the entire water column. For the RT90 case, the red upper beam is narrower than the downward beam.

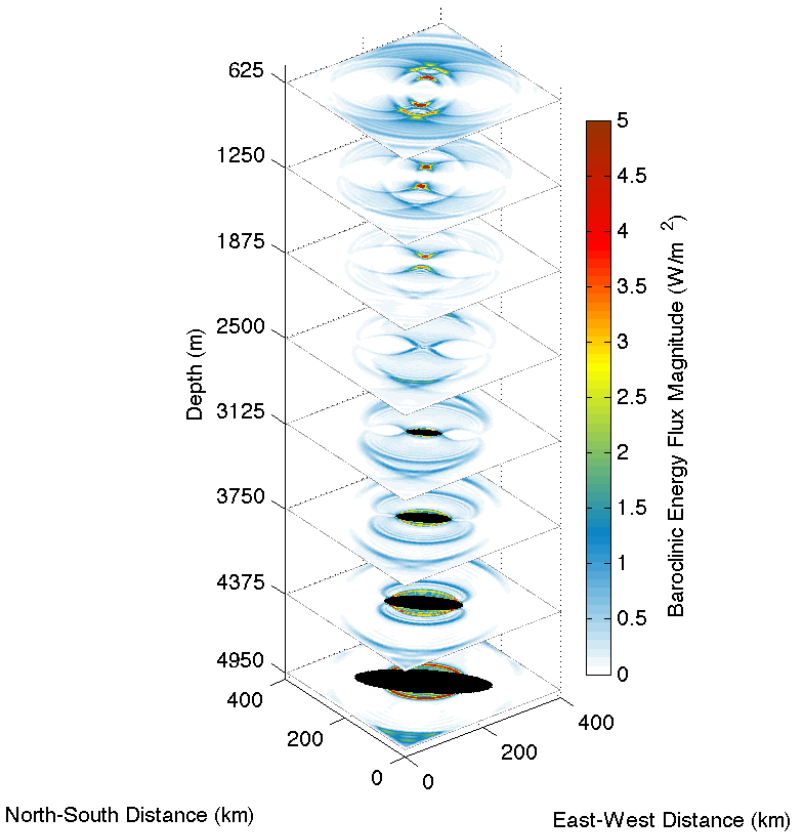

Figure 2.3. Horizontal cross-sections of baroclinic energy flux magnitude for the RT90 case, where the rectilinear tide is perpendicular to the major axis of a 3:1 ridge. Energy radiates both upward and downward away from the ridge top. The energy flux is particularly intense above the ridge due to the focusing affect the curvature of the ridge has on energy propagating upward from the critical areas near the ridge crest.

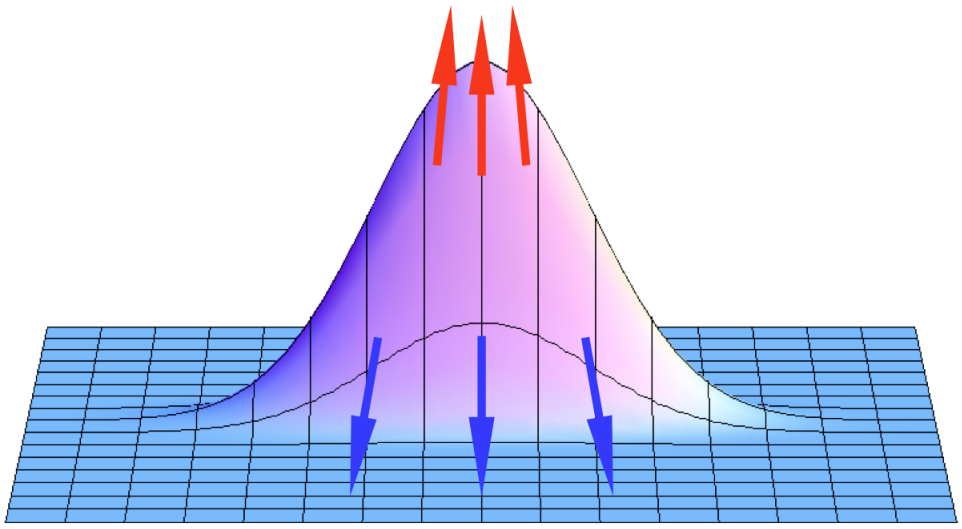

Figure 2.4. Schematic showing the direction of the gradient near the ridge crest. Red vectors point up while blue vectors point down along the maximum slope, illustrating the convergence of the upward beams. Energy flux radiates upward and downward from a convex critical area near the ridge crest. Because of the curvature of the 3:1 ridge, the energy flux propagating upward and over the ridge crest is focused above the ridge, while the downward energy flux vectors fan out in a widening arc away from the ridge.

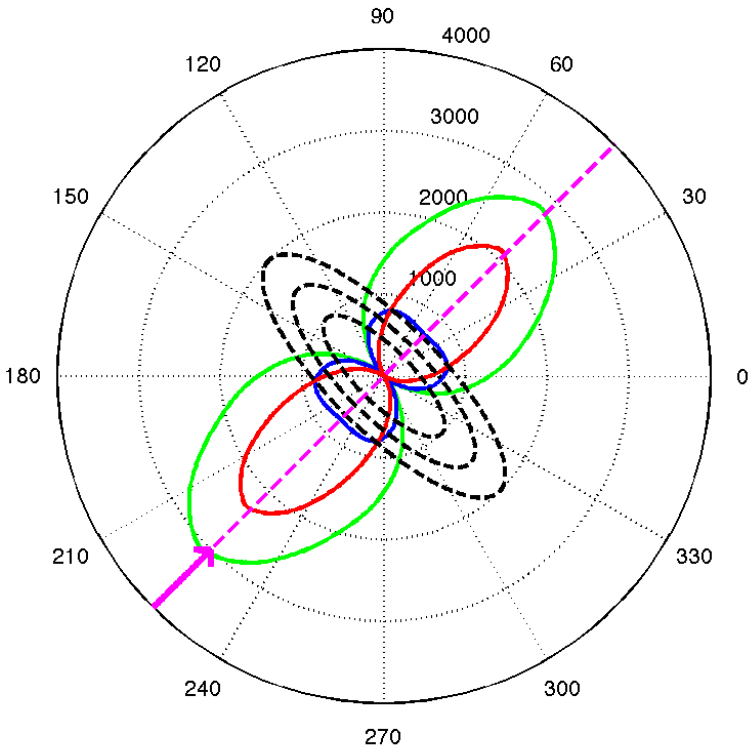

Figure 2.5. Upward (red), downward (blue), and total (green) depth-integrated normal energy flux as a function of azimuthal angle out of circular cylinders of radius 100 km in the upper half, lower half, and entire water column for the RT90 case. The dashed black lines are ridge contours intended only to show the orientation of the ridge to the tide; the radial scale is the magnitude of energy flux. Most of the energy flux is concentrated on the near and far sides of the ridge parallel to the propagation of the tide. At this particular cylinder radius, the pattern of energy flux in the upper half of the water column is narrower due to the focused nature of the upward beam near the ridge and the angular spreading in the downward beam.

Chapter 3

Rectilinear Tide

3.1 Energy Flux vs. Relative Incidence Angle

Here we present results for barotropic to baroclinic energy conversion as a function of relative incidence angle (RIA). The baroclinic energy flux at a ridge was analyzed for nine values of RIA between 90° (the perpendicular case) and 0° (the parallel case) (Fig. 3.1). The Coriolis parameter is zero in all of these runs and the RIA between the tide and the longer ridge axis is varied in increments of 11.25° between model runs by rotating the ridge orientation and keeping the tide direction constant. Initially, the directions of maximum outward normal flux remain nearly perpendicular to the semi-major axis and a significant fraction of the perpendicular regime's energy is radiated away. As the RIA is reduced, the radiated energy begins decreasing dramatically and the narrow upward beam becomes less focused. As the RIA is reduced from 11.25° to 0°, the flux pattern is rapidly distorted and realigns with the direction of the tide, rather than the normal direction to the ridge. This parallel case is the weakest generator of baroclinic energy flux.

3.2 Directivity vs. RIA

First, we describe the focusing of the upward beam over the crest of the ridge. The narrowness of the different beam patterns is described by computing their directivity D. This quantity, used to quantify transducer or antenna performance, is the ratio of maximum intensity at any direction

divided by the average intensity over all directions (Medwin and Blue, 2005). By definition, D must be greater than or equal to one; an omnidirectional source has $D = 1$, while a delta function source would have $D \to \infty$. Here, D vs. RIA is calculated as the ratio of maximum depth-integrated outward normal energy flux E_{max} to the depth-integrated outward normal energy flux averaged over

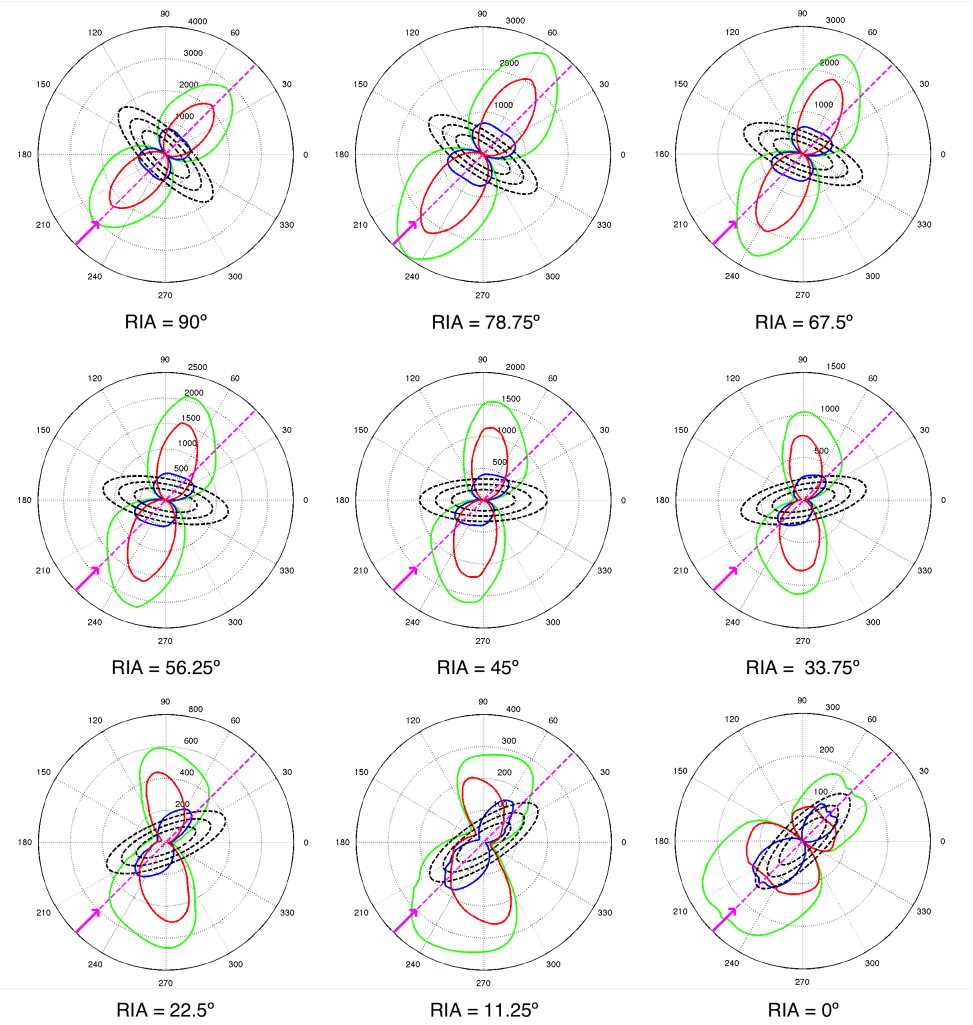

Figure 3.1. A panel of cases showing depth-integrated normal energy flux out the walls of cylinders in the upper half of the water column (red), the lower half of the water column (blue), and the entire water column (green) at RIA values from $90°$to $0°$. As the RIA is reduced, the energy flux produced decreases, but near-perpendicular orientations are still efficient generators of baroclinic energy. The beam pattern remains nearly locked to the ridge, such that the azimuth of the peak energy flux is nearly perpendicular to the long axis of the ridge, until the RIA reaches $0°$ and the beam pattern is significantly distorted.

the azimuthal direction $\langle E \rangle_\phi$:

$$D = \frac{E_{max}}{\langle E \rangle_\phi}. \tag{3.2.1}$$

Using directivity to describe the shape of the beam pattern created by this ridge would be best applied in the farfield situation, where we would expect less variation of the pattern with distance from the ridge. However, the focused energy flux immediately above the ridge was very much a nearfield effect. To highlight this feature while maintaining some consistency in applying the formula, the directivity is consistently calculated at 100 km from the ridge, just outside the region of baroclinic energy flux generation. Figure 3.2 shows that the directivity of the upper energy pattern is higher at higher RIA values near the perpendicular case, where upward energy flux is focused above the ridge, while the lower beam shows the opposite trend. In that case, the parallel ridge presents a subcritical slope to the tide, and the resulting energy flux is peaked near the ends of the ridge.

3.3 Perpendicular and Parallel Regimes

The total power at a given RIA is calculated by integrating the outward normal baroclinic energy flux at a distance of 100 km from the ridge over both the depth and azimuthal dimensions (Fig. 3.3). The red and blue curves represent the upper and lower halves of the water column, while the green curve shows the radiated power of the entire water column. The perpendicular regime (RIA = 90°) is seen to produce nearly one order of magnitude more than the power than the parallel regime (RIA = 0°).

The numerical results are compared to a theoretical estimate obtained by hypothesizing that the energy flux is the sum of the effects of the parallel and perpendicular regimes. By decomposing the tidal velocity into components perpendicular to and parallel to the ridge's longer axis, and estimating that the total energy flux from each regime is proportional to the square of the velocity component in that direction, then the magnitude of the total energy flux E may be found from the energy flux in the two regimes and the RIA. These calculations for the upper, lower and combined

beams are shown as the three black dashed curves in Figure 3.3, given by

$$E(\phi) = E_{\perp} \cdot \sin^2 \phi + E_{\parallel} \cdot \cos^2 \phi, \tag{3.3.1}$$

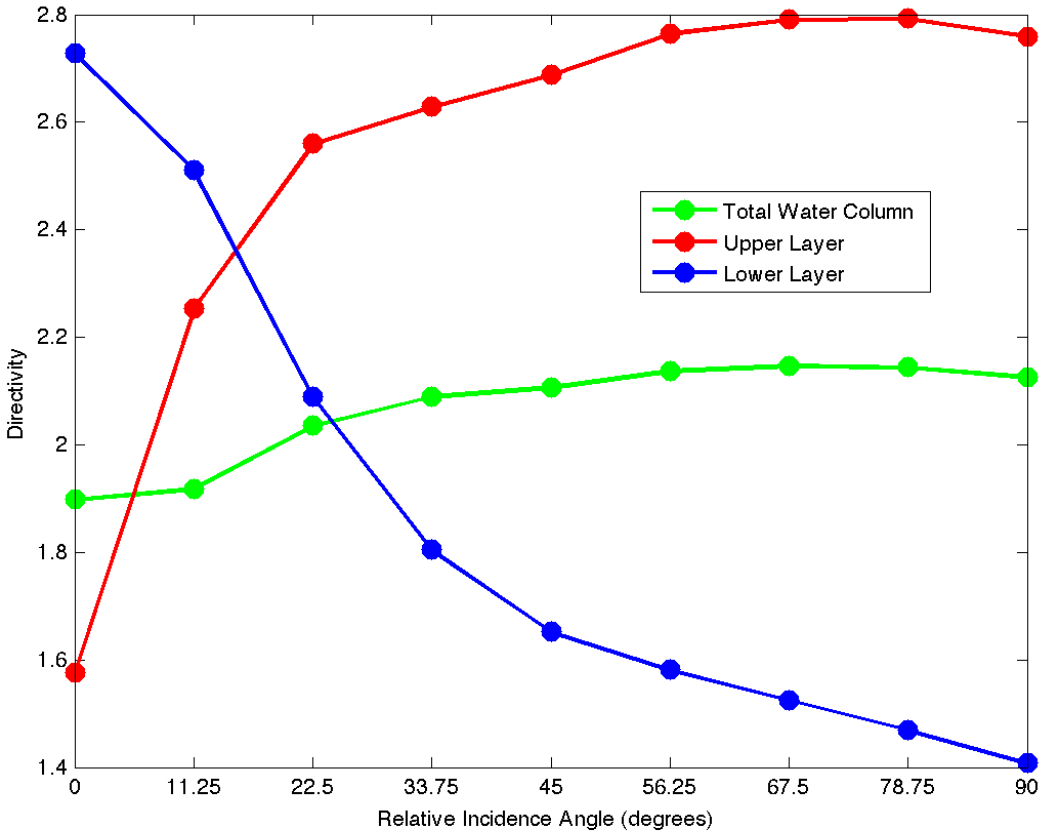

Figure 3.2. Directivity vs. RIA for the depth-averaged normal energy flux out of the upper half of the water column (red), lower half (blue), and the entire water column (green) evaluated at 100 km from the ridge. The red curve of directivity in the upper half is larger near the perpendicular regime, illustrating the focusing of the upward beams radiating away from the critical area near the ridge crest. The blue curve of directivity in the lower half of the water column shows the opposite effect: the energy flux is more evenly distributed in all directions in the perpendicular case, but is more concentrated at certain directions in the parallel regime where the ridge is subcritical to the tidal flow. In this latter case, the ends of the ridge show intense patches of energy flux not seen in the RT90 case.

where ϕ is the RIA, $E_\perp$ is the energy flux from the perpendicular regime and $E_\parallel$ is the energy flux from the parallel regime. The excellent agreement between the black curves and the model run results suggest that the radiated power at an arbitrary RIA can be well-estimated from this empirical formula and the results of the two end regimes. The next section presents a more physical basis for this result.

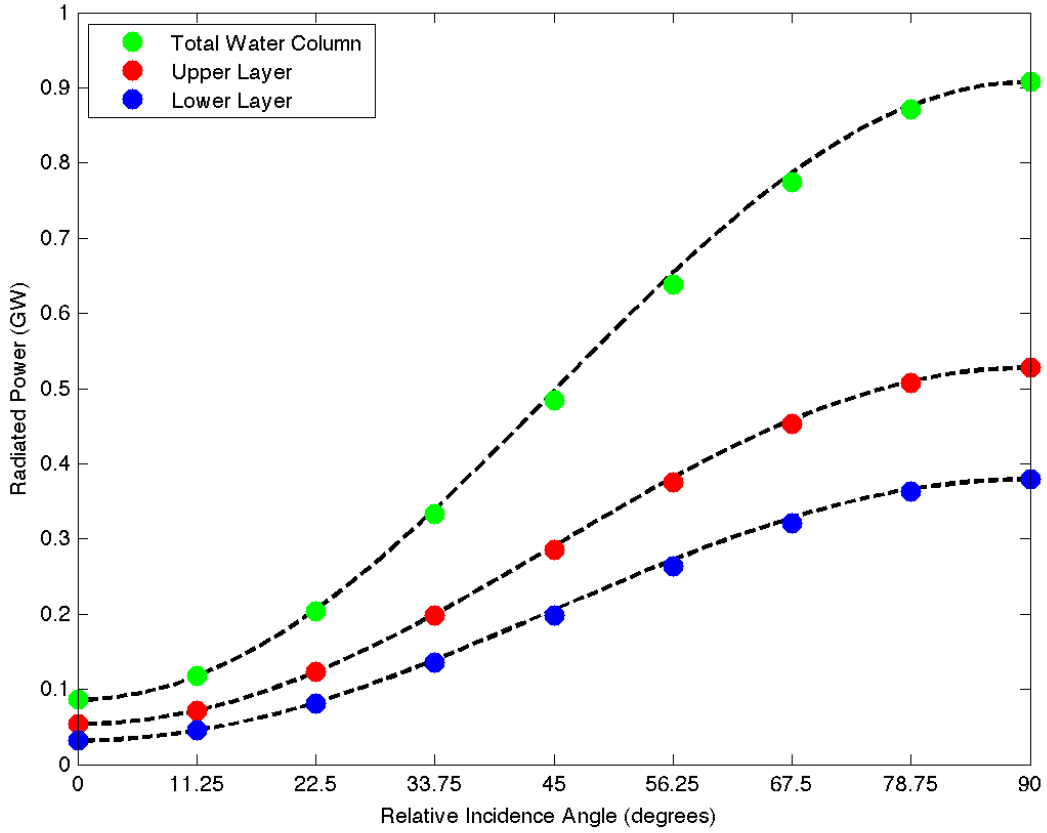

Figure 3.3. Energy flux vs. RIA without rotation ($f = 0$). The green, red, and blue data points from the numerical model show the energy flux out the control volume for the total, upper half, and lower half of the water column, respectively. The empirical relations (dashed lines) for these same three control volumes are also plotted, fit to the parallel and perpendicular endpoint cases. The empirical relations are excellent at predicting the energy flux at an arbitrary RIA.

3.4 Energy Flux Prediction

The boundary condition for internal tide generation motivates an explanation of the empirical formula of the previous section. The generation of baroclinic energy at a Gaussian-shaped undersea ridge is driven by the bottom boundary condition in an idealized baroclinic generation scenario:

$$w|_{z=h} = \vec{u} \cdot \nabla h, \tag{3.4.1}$$

(Llewellyn Smith and Young, 2002). The dot product allows this to be interpreted two ways: either the vertical velocity depends on the component of velocity in the direction of the steepest slope (the gradient), or the vertical velocity at a location depends on the directional derivative parallel to the current flow; both interpretations are equivalent. The latter interpretation is adopted here. In addition, we also expect more generation when a ridge presents a significant obstacle to a barotropic tide (Holloway and Merrifield, 1999). This can be represented by the projected area of the ridge in a vertical two-dimensional plane perpendicular to the surface tide's direction of propagation.

These ideas motivate our assumption that the generated baroclinic energy flux E is approximately proportional to both the projected area σ and the maximum topographic slope s_{max} in the direction of the background surface tidal flow as follows:

$$E \propto s_{max} \cdot \sigma. \tag{3.4.2}$$

This assumption captures both the impact that the effective slope has on generation, but also quantifies the blocking effect, where elongated topography prevents barotropic flow from diverting around a feature. Holloway and Merrifield (1999) show that both the blocking effect and the slope are important factors in baroclinic generation.

While this may be a simplistic assumption, when expressed in terms of the ridge parameters, it matches our results well. A submarine ridge with an elliptical horizontal cross-section and a

Gaussian vertical cross-section has a height h given by:

$$h = H_0 e^{-(x^2/A^2 + y^2/B^2)}, \tag{3.4.3}$$

where H_0 is the maximum height of the ridge above the seafloor and A and B are measures of the horizontal length scales of the ridge in the x and y directions. At a height h above the seafloor, this makes an ellipse in the xy plane with semi-minor and semi-major axes a and b respectively, given by

$$a = A\sqrt{\ln(H_0/h)} \quad \text{and} \tag{3.4.4}$$

$$b = B\sqrt{\ln(H_0/h)}. \tag{3.4.5}$$

Using a parameter t that spans 0 to 2π allows x and y to be represented as:

$$x = a\sin t \quad \text{and} \tag{3.4.6}$$

$$y = b\cos t. \tag{3.4.7}$$

To represent an incoming tide at an arbitrary angle to the coordinate system, we define new coordinates x' and y' rotated counterclockwise by the angle $90° - \phi$ from the original coordinates, making the ϕ the RIA:

$$x' = x\sin\phi + y\cos\phi \quad \text{and} \tag{3.4.8}$$

$$y' = -x\cos\phi + y\sin\phi. \tag{3.4.9}$$

So the parametrized ellipse can be written as

$$x' = a\sin\phi\sin t + b\cos\phi\cos t \quad \text{and} \tag{3.4.10}$$

$$y' = -a\cos\phi\sin t + b\sin\phi\cos t. \tag{3.4.11}$$

To find the effective or projected area of the ellipse when the tide approaches from the positive x' axis, we first find the y' values where the tangent line to the ellipse is parallel to the x' axis by finding the values t^* that satisfy

$$\frac{\partial y'}{\partial t} = -a\cos\phi\cos t^* + -b\sin\phi\sin t^* = 0. \tag{3.4.12}$$

These are given by

$$\sin t^* = -\frac{a\cos\phi}{\sqrt{a^2\sin^2\phi + b^2\cos^2\phi}} \quad \text{and} \tag{3.4.13}$$

$$\cos t^* = \frac{b\sin\phi}{\sqrt{a^2\sin^2\phi + b^2\cos^2\phi}}. \tag{3.4.14}$$

The extreme values of y' at these values of t^* then are

$$y' = \pm\sqrt{a^2\cos^2\phi + b^2\sin^2\phi}. \tag{3.4.15}$$

Defining the effective or projected width scale of the ridge to be $C = \sqrt{A^2\sin^2\phi + B^2\cos^2\phi}$, we find that the silhouette of the ridge is given by

$$h = H_0 e^{-y'^2/C^2}. \tag{3.4.16}$$

The profile or silhouette of the 3-D Gaussian ridge with an elliptical horizontal cross-section, rotated by an angle ϕ from an observer, is just a 2-D Gaussian ridge, with an effective width scale C that depends on ϕ. If $\phi = 90°$, $C = B$, so the ridge looks like a 2-D Gaussian with the shape $h_0 = H_0 e^{-y'^2/B^2}$. If $\phi = 0°$, $C = A$, so the ridge just looks like a narrower 2-D Gaussian with the shape $h = H_0 e^{-y'^2/A^2}$. At an arbitrary RIA, C is in between A and B, so the profile is "in between" the two extremes. The area σ of the silhouette is the integral

$$\sigma = \int_{-\infty}^{+\infty} h\, dy' = H_0 C\sqrt{\pi}. \tag{3.4.17}$$

The end cases are when the ridge is perpendicular or parallel to the tide. In the perpendicular case, $C = B$ and

$$\sigma_\perp = H_0 B\sqrt{\pi}. \tag{3.4.18}$$

In the parallel case, $C = A$ and

$$\sigma_\parallel = H_0 A\sqrt{\pi}. \tag{3.4.19}$$

The area at an arbitrary RIA may then be written as a function of these end cases:

$$\sigma^2 = \sigma_\parallel^2 \sin^2\phi + \sigma_\perp^2 \cos^2\phi. \tag{3.4.20}$$

In fact, this result is not unique to a Gaussian ridge. As long as horizontal cross-sections are ellipses, making the height h a function of the quantity $q = x^2/A^2 + y^2/B^2$, the silhouette h of the projected ridge has the equivalent 2D shape, making the silhouette a function of the parameter $-y'^2/C^2$ where C is the same effective width given above. The projected area will be $\sigma = H_0 CF$, where the proportionality F is $\sqrt{\pi}$ for the Gaussian, π for the popular "Witch of Agnesi" ridge, and 1 for an elliptical cone.

For a given ridge, the square of the effective ridge area (3.4.20) scales similarly to the baroclinic energy flux generated by the ridge when the RIA is varied (3.3.1). This peculiar result suggests the energy flux is proportional to the square of the area of the silhouette of the ridge, but two-dimensional studies such as St. Laurent et al. (2003) and Llewellyn Smith and Young (2003) naturally show that the conversion is independent of the third dimension. Extrapolating this result, the conversion per unit of ridge width at an infinite ridge should be independent of the width, while the conversion at long ridges should become proportional to the ridge width.

The resolution to this quandary comes from the inclusion of the topographic slope. Llewellyn Smith and Young (2002) show that the conversion over infinitely long subcritical slopes depends in

general on the width of the ridge in the direction of tidal flow, but that in the limit of an infinitely deep ocean, reproducing the results of Bell (1975a), the width no longer affects the solution.

If the tide flows parallel to the unit vector $\hat{v} = -\sin\phi\hat{x} - \cos\phi\hat{y}$ (parallel to the surface tide propagating from the positive $\hat{x'}$ direction to the negative $\hat{x'}$ direction, then the slope s of the ridge along this direction is given by

$$s = -\sin\phi \cdot \frac{\partial h}{\partial x} - \cos\phi \cdot \frac{\partial h}{\partial y}. \tag{3.4.21}$$

If we again allow the ridge to be any function of the ellipse parameter $q = x^2/A^2 + y^2/B^2$, we then may rewrite the slope as

$$s = -2\frac{\partial h}{\partial q}\left(\frac{x\sin\phi}{A^2} + \frac{y\cos\phi}{B^2}\right). \tag{3.4.22}$$

The maximum slope occurs where $\nabla s = 0$, $\nabla = \hat{x} \cdot \frac{\partial}{\partial x} + \hat{y} \cdot \frac{\partial}{\partial y}$, so both of the components of ∇s are zero.

$$\frac{\partial s}{\partial x} = -2\frac{\partial^2 h}{\partial q^2}\frac{2x}{A^2}\left(\frac{x\sin\phi}{A^2} + \frac{y\cos\phi}{B^2}\right) - 2\frac{\partial h}{\partial q}\left(\frac{\sin\phi}{A^2}\right) = 0 \quad \text{and} \tag{3.4.23}$$

$$\frac{\partial s}{\partial y} = -2\frac{\partial^2 h}{\partial q^2}\frac{2y}{B^2}\left(\frac{x\sin\phi}{A^2} + \frac{y\cos\phi}{B^2}\right) - 2\frac{\partial h}{\partial q}\left(\frac{\cos\phi}{B^2}\right) = 0. \tag{3.4.24}$$

This determines the point or points (x, y) where the slope is at a maximum. One useful result comes from evaluating

$$x\frac{\partial s}{\partial x} + y\frac{\partial s}{\partial y} = \left[-2\frac{\partial^2 h}{\partial q^2}\left(\frac{x^2}{A^2} + \frac{y^2}{B^2}\right) - \frac{\partial h}{\partial q}\right] \cdot \left(\frac{x\sin\phi}{A^2} + \frac{y\cos\phi}{B^2}\right) = 0. \tag{3.4.25}$$

The ridge slope is a maximum when the quantity in square brackets is zero, or the second factor in parentheses is zero, or both factors are zero. As the second factor is also a factor in the slope s itself, if the second factor is zero, the slope is identically zero everywhere, so this possibility is rejected and the quantity in square brackets must be zero when the slope is at a maximum. This quantity includes the ellipse parameter $q = x^2/A^2 + y^2/B^2$. For certain ridge shapes, it defines a particular

ellipse for the type of ridge involved. Rearranging it yields the value

$$Q = \left(\frac{x^2}{A^2} + \frac{y^2}{B^2}\right) = -\frac{1}{2} \cdot \frac{\frac{\partial h}{\partial q}}{\frac{\partial^2 h}{\partial q^2}}. \tag{3.4.26}$$

The right-hand side is generally a constant, a quantity unique to each ridge shape. For a Gaussian ridge, $Q = 1/2$. For a Witch of Agnesi, $Q = 1/3$. For an elliptical cone, this reduces to the identity $Q = q$, so no new information is given; the steepest slope of a cone approached from a certain direction does not fall on a particular ellipse.

Another useful expression for determining the maximum slope is

$$\frac{\partial s}{\partial x}\sin\phi + \frac{\partial s}{\partial y}\cos\phi = 0 \tag{3.4.27}$$

$$= -2\left(2\frac{\partial^2 h}{\partial q^2}\left(\frac{x\sin\phi}{A^2} + \frac{y\cos\phi}{B^2}\right)^2 + \frac{\partial h}{\partial q}\left(\frac{\sin^2\phi}{A^2} + \frac{cos^2\phi}{B^2}\right)\right) \tag{3.4.28}$$

From this we find

$$\frac{x\sin\phi}{A^2} + \frac{y\cos\phi}{B^2} = \frac{\sqrt{Q}C}{AB}. \tag{3.4.29}$$

Hence the maximum slope s_{max} may be simplified to

$$s_{max} = -2\left(\frac{\partial h}{\partial q}|_{q=Q}\right)\frac{\sqrt{Q}C}{AB}. \tag{3.4.30}$$

The quantity $\frac{\partial h}{\partial q}$ introduces a factor of H_0, the ridge height, making the maximum ridge slope dependent on this height and the length scales A, B, and C, where the proportionality depends on the type of ridge:

$$s_{max} \propto \frac{H_0 C}{AB}. \tag{3.4.31}$$

Since the projected ridge area σ is given by 3.4.17,

$$\sigma \propto H_0 C, \tag{3.4.32}$$

assuming that the baroclinic energy flux E is proportional to both the projected area and the maximum slope leads to the conclusion that

$$E \propto \frac{H_0^2 C^2}{AB} = \frac{H_0^2 \left(A^2 \cos^2 \phi + B^2 \sin^2 \phi\right)}{AB}. \tag{3.4.33}$$

This shows that for the perpendicular or parallel cases, the flux will scale with the square of the effective ridge area. The effective area is the effective width times the ridge height. Figure 3.4 shows that the flux is linear with the square of ridge area for perpendicular ridges, consistent with Equation 3.4.33. For ridges with elliptical cross-sections, C^2/AB appears to be the non-dimensional parameter controlling the effects of both the ridge dimensions and orientation of the tide on the baroclinic generation. With this result, the generation at arbitrary incidence angles can be predicted from the generation at a known orientation. The generation per width at an infinite ridge, where the tide is perpendicular to the ridge (a 2D problem) and the maximum slope is the same as the finite ridge case, is given by

$$E_\infty = \frac{E}{B} \propto \frac{H_0^2}{A}. \tag{3.4.34}$$

Then the generation over a finite ridge at an arbitrary RIA becomes

$$E \propto \frac{E_\infty C^2}{B}. \tag{3.4.35}$$

Similarly, if the generation in the perpendicular case at a finite ridge is known, the generation at an arbitrary angle to that same ridge is

$$E \propto \frac{E_\perp C^2}{B^2} = \frac{E_\perp \left(A^2 \cos^2 \phi + B^2 \sin^2 \phi\right)}{B^2}. \tag{3.4.36}$$

Rotating the ridge away from the RT90 case presents a more gradual slope to the barotropic flow. The baroclinic energy flux generated by the model with a 3:1 ridge of fixed dimensions and RIA values from $\phi = 0^\circ$ to $\phi = 90^\circ$ is shown in Figure 3.5. The same figure also shows the results from ridges perpendicular to the flow with the same effective slope and effective area as the rotated ridge. Since $\phi = 90^\circ$ for all the points on this curve, the effective slope and area are matched to the rotated case by varying both horizontal length scales A and B: the perpendicular ridge will

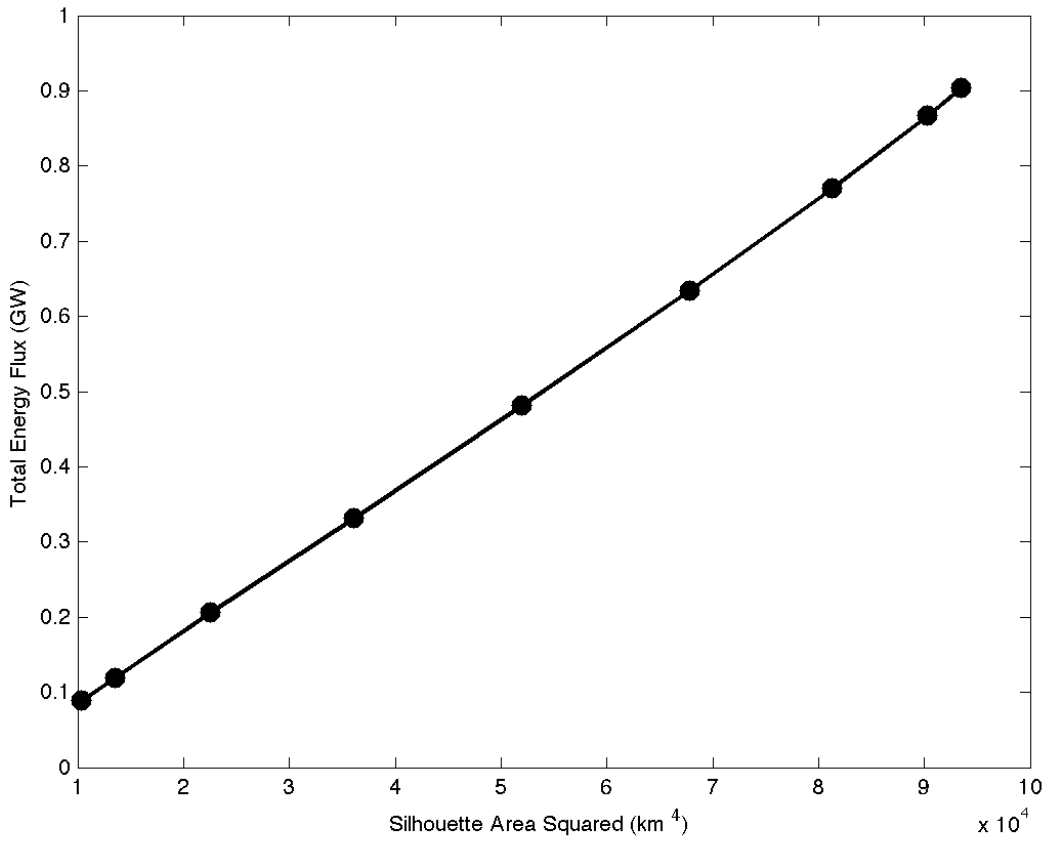

Figure 3.4. Baroclinic energy flux from a single ridge is shown vs. the square of that ridge's effective area, as in Eqn: 3.4.33 with A and B fixed while ϕ varies. In this case, the energy flux will seem to vary with the square of the effective area given in Eqn: 3.4.32. The area is changed by rotating the RIA between the ridge and the tide, altering the effective width C and therefore both the effective area and the maximum slope. The horizontal length scales A and B are kept constant. The linear relationship shows, for the perpendicular ridge orientation, that the energy flux is proportional to the square of the effective area.

have a shorter scale B and a wider scale A than the oblique ridge, so a perpendicular ridge must be more nearly circular than an oblique ridge to generate the same energy flux. In practice, the effective perpendicular ridge actually produces more baroclinic energy flux than the oblique ridge it simulates. Equivalently, Eqn. 3.4.33 overestimates the energy flux generated by an oblique ridge, possibly by poorly representing the ability for the barotropic flow to divert around the oblique ridge, or by the simplified assumption that the maximum slope represents the energy flux generated by the entire ridge. The two curves have a similar shape, showing that rotating a ridge away from the perpendicular case decreases the baroclinic energy flux produced by essentially reducing the slope and area of that ridge as experienced by the surface tide. In the perpendicular RT90 case, the energy flux is proportional to the aspect ratio, or the major axis length scale B if A is fixed:

$$E \propto H_0^2 \frac{B}{A}. \tag{3.4.37}$$

A linear (but not directly proportional) relationship between the baroclinic energy flux and the ridge's major length scale B is displayed in Figure 3.6; however, the proportionality must change as the length scale shortens (making the slope increasingly supercritical) so that the generated flux will vanish as the ridge's horizontal scale goes to zero, since a knife-edge barrier parallel to the tide would generated no internal energy. Our simple relationship for energy flux is not valid for the most supercritical slopes where $\epsilon \gtrsim 3$. Finally, we note that in the case of a circularly symmetric seamount, $A = B = C$, so that the predicted energy flux naturally becomes independent of the RIA. Our simple formula estimating energy flux predicts

$$E \propto H_0^2, \tag{3.4.38}$$

so that the flux generated by seamounts is independent of their horizontal extent. In Figure 3.7, the energy flux is seen to be fairly constant for larger seamounts of radius 46.5 km and larger, but the approximation in 3.4.38 completely overestimates the flux generated by steeper pinnacles with smaller radii; namely seamounts more supercritical than $\epsilon \simeq 1.1$. It is evident that estimating the blocking using only the effective area is overly optimistic for these supercritical cases, so it is likely

that the barotropic flow almost entirely bypasses the seamount to the sides rather than passing over the top, resulting in less energy flux. It is interesting that the breakdown of the empirical formula for energy flux in Eqn. 3.3.1 manifests itself here with barely supercritical circular seamounts, but that the linear relationship predicted by the empirical formula with elongated ridges perpendicular to the tide in Figure 3.6 held up for high values of slope criticality. Evidently the empirical formula

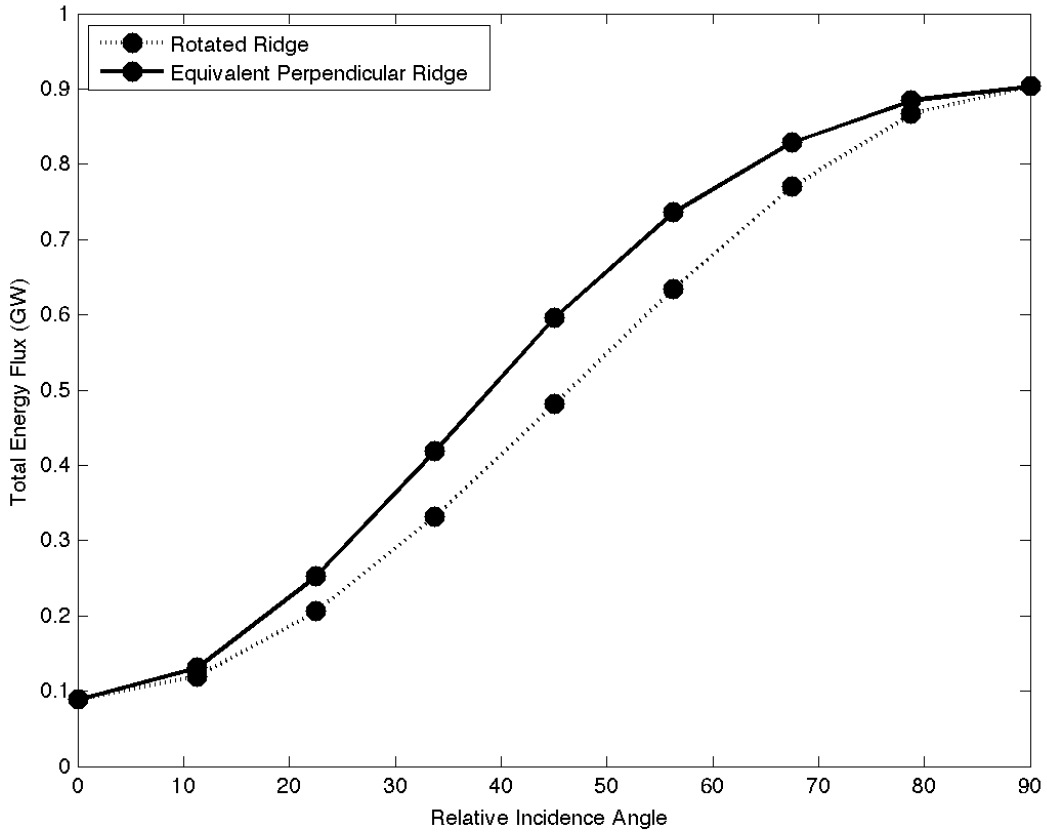

Figure 3.5. Baroclinic energy flux generated by two different methods of changing the effective area and effective slope. The points along the dotted curve are generated by model runs of tidal flow over a 3:1 ridge at RIA values between $0°$ and $90°$, connected by the empirical formula given in Eqn. 3.3.1 predicting energy flux at an arbitrary RIA. The points connected by straight solid segments are generated by model runs of tidal flow over ridge always perpendicular to the tide. These ridges have the same effective area and effective slope as the 3:1 ridge at that corresponding RIA. Achieving the same effective area and effective slope while keeping a perpendicular RIA is accomplished by changing the horizontal scales A and B. The resulting energy flux between the two methods is similar, suggesting that the RIA is important because it changes the effective area and slope.

is poorest at estimating the generation at circular seamounts, which seems sensible because the diversion of the surface tide around the topography is most significant for seamounts rather than ridges perpendicular to the tide.

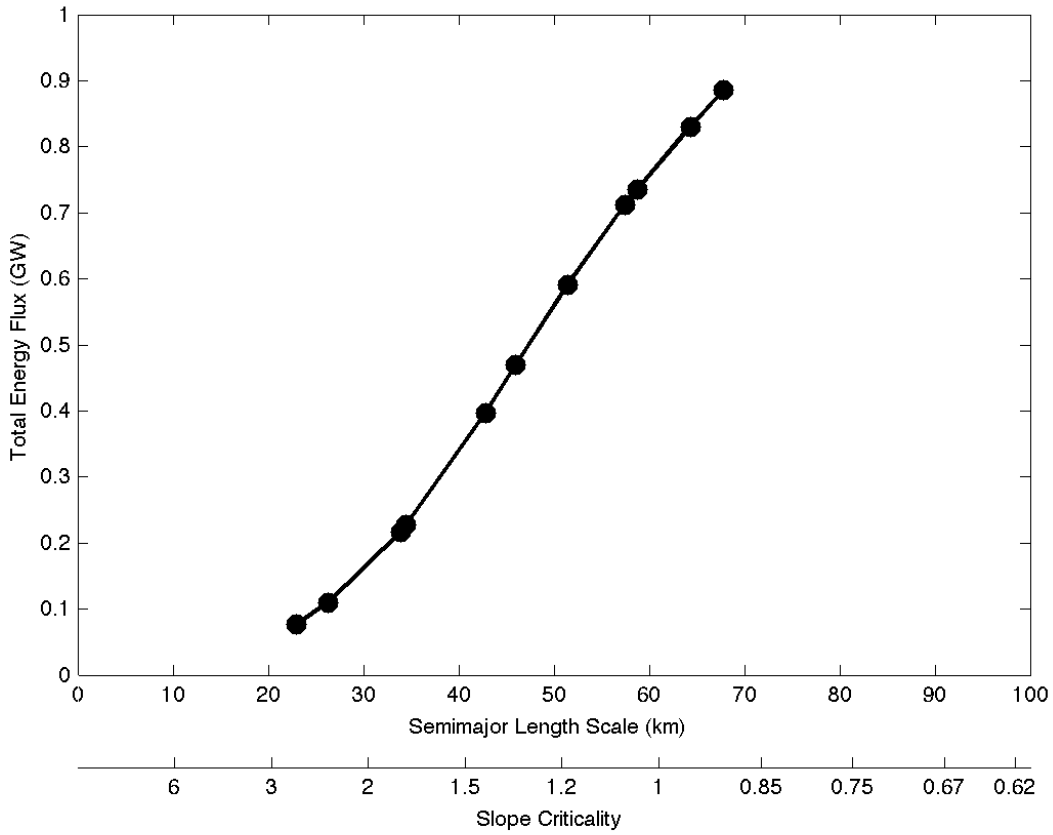

Figure 3.6. Baroclinic energy flux generated with perpendicular tidal flow for different aspect ratios. In the special perpendicular case, changing the semi major horizontal length scale B has no impact on the effective slope, only the effective area. Here, the total energy flux is a roughly linear function of B, but in order to intercept the origin the curve must bend significantly for shorter values of B, so the relationship is more complicated for steep, small-scale seamounts.

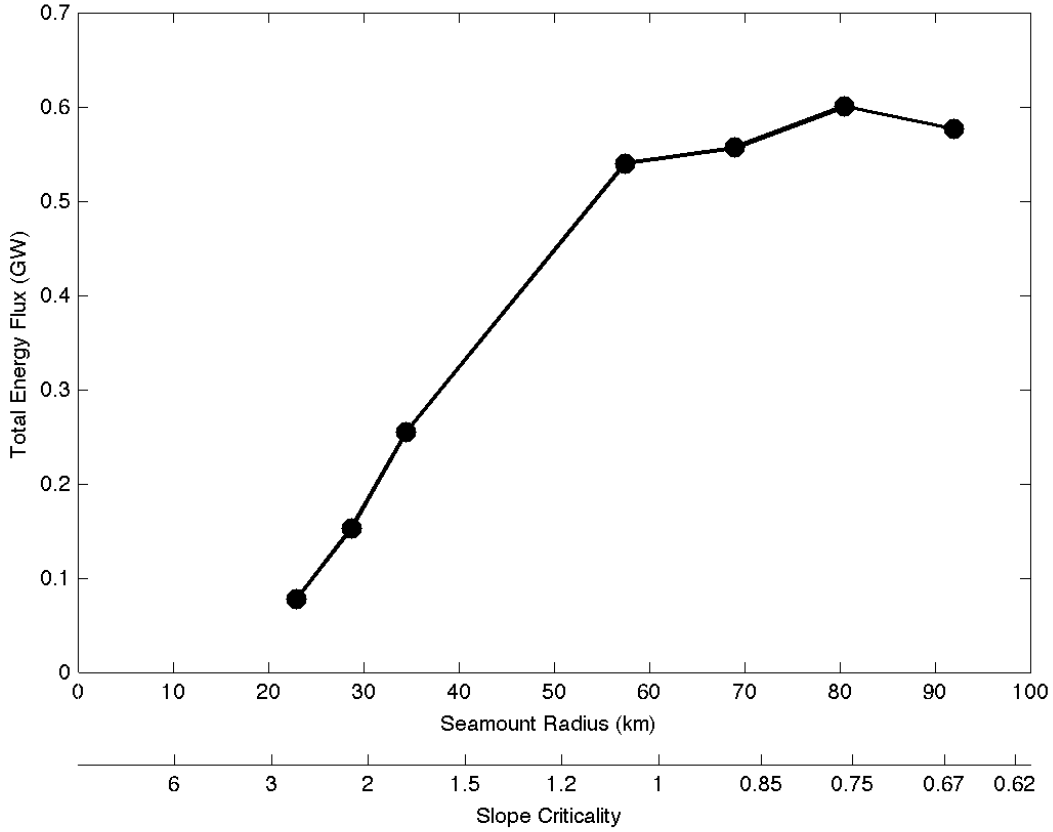

Figure 3.7. Baroclinic energy flux generated with perpendicular tidal flow for different sized circularly symmetric seamounts. In this case the horizontal scales A and B and the effective width C are all equal; they are the radius of the seamount. The simple empirical formula predicts the energy flux created by such a ridge should be independent of the radius. While the result is nearly constant at longer radii, it fails for shorter values. Steep, narrow pinnacle-like seamounts are extremely poor generators of baroclinic energy.

Chapter 4

Rotating Tide

4.1 Effects of Rotation on Energy Flux

In the previous section, we considered model runs where the rectilinear tide propagated without the effect of rotation. When rotation is incorporated into the wave dynamics, the Poincare wave's barotropic tidal current sweeps out an ellipse every tidal cycle, depending on the nature and number of waves involved. For example, a single Poincare wave (rotating surface gravity wave) would be rectilinear at the equator, circular at the turning latitude for that frequency, and elliptical at latitudes in between. On the other hand, a Kelvin wave propagating along a straight coastline would be rectilinear. In the real ocean, the eccentricity of the tidal ellipse at a given location may not be predictable from just the latitude; it is generally the superposition of all the waves passing through that point (Fig. 6 of Kantha (1995)).

In this study, we introduce rotation by specifying a non-zero Coriolis parameter, making our shallow water surface tide with rectilinear currents into a Poincare wave with elliptical tidal currents. This method also affects the numerical simulation by introducing the Coriolis parameter into the primitive equations in the model domain interior. In order to determine which change has the more significant effect on baroclinic energy flux generation, two test model runs were performed. The first used an elliptical surface tide for the forcing, but maintained $f = 0$ in the interior dynamics. The second used a rectilinear surface tide for the forcing, but introduced a non-zero f in the interior. The generated baroclinic energy flux for the first test case with elliptical tidal forcing but $f = 0$ in

the interior matches within 1% of the same scenario with rotation in the forcing and the interior, while the second test case's energy flux generation was very similar to the results with no rotational dynamics whatsoever. Clearly the elliptical tidal currents are responsible for the change in the baroclinic energy flux caused by including rotation in the dynamics.

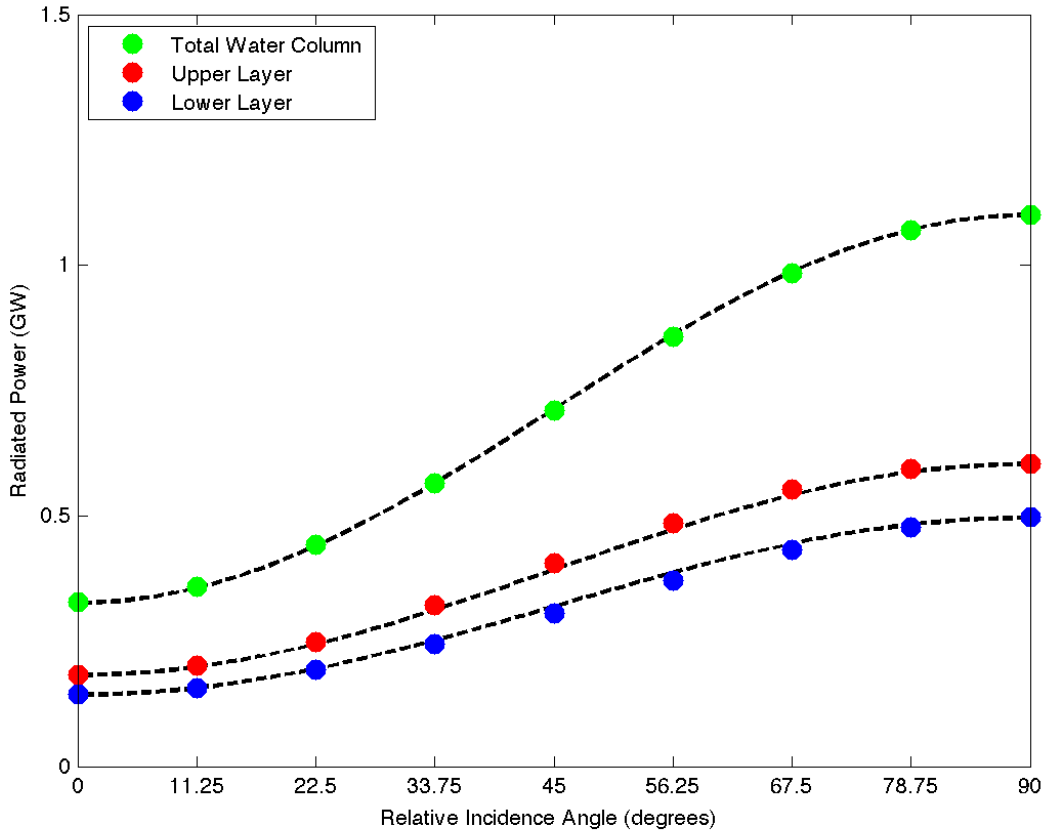

Figure 4.1. Energy flux vs. RIA for a 3:1 ridge forced by a Poincare wave with $f = 0.5581 \cdot 10^{-4}$ rad/s. The result is similar to Figure 3.3, although more energy flux is produced (note the increase in scale). The energy flux at an arbitrary RIA is still well-predicted by the empirical formula.

When elliptical tidal forcing is used in the model, two differences between the rotating cases, shown in Figures 4.1, 4.2, and 4.3, and the non-rotating case, shown in Figure 3.3, are immediately evident: more energy flux is produced in the rotating cases, and the energy flux there is less sensitive to the RIA. It should be noted that the forcing wave's dynamics have been altered, but while the introduction of rotation has altered the partition of kinetic and potential energy, the

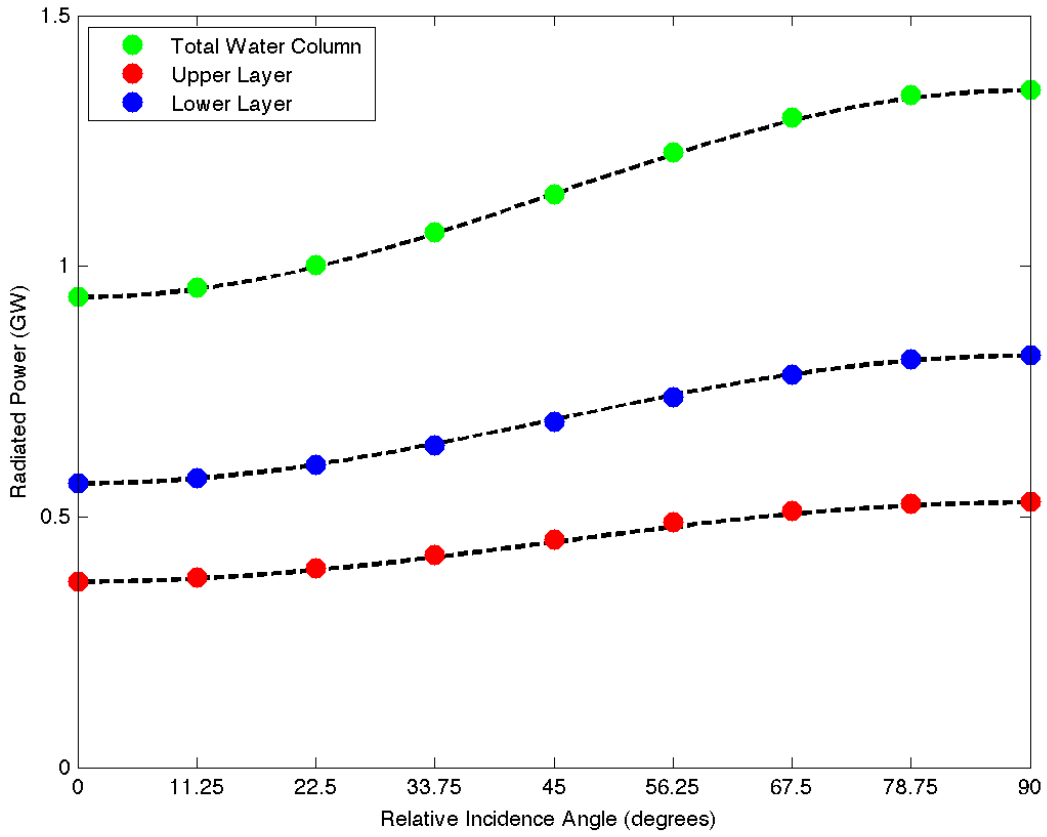

Figure 4.2. Energy flux vs. RIA for a 3:1 ridge forced by a Poincare wave with $f = 1.0313 \cdot 10^{-4}$ rad/s. At any particular RIA, the energy flux with this elliptical tide is larger than for a rectilinear tide and still well-predicted by the empirical formula. The resulting energy flux is also less sensitive to the RIA than with a rectilinear tide.

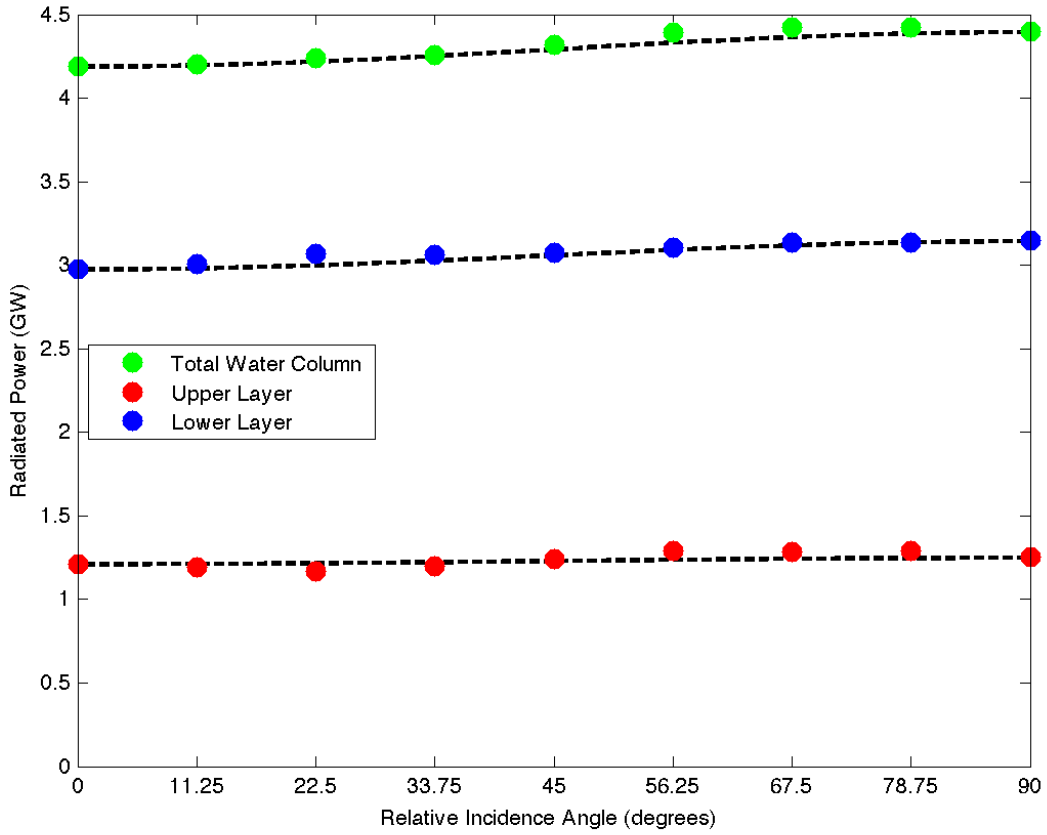

Figure 4.3. Energy flux vs. RIA for a 3:1 ridge forced by a Poincare wave with $f = 1.3474 \cdot 10^{-4}$ rad/s. With a nearly circular tidal velocity forcing the model, the result is nearly independent of the RIA, since for any orientation of the ridge to the tide's wave vector, there is some phase of the tide where a significant velocity flows perpendicular to the ridge. As a result, the scale of the energy flux produced is also increasing significantly.

total energy (averaged over a wave cycle) remains unchanged for the same frequency and current magnitude (Gill, 1982).

In the rotating case, the tidal current velocity is nonzero at every phase, whereas in the non-rotating case, the current went to zero twice every tidal cycle. This creates more opportunities for the steep topography to deflect the barotropic current upward, triggering internal waves. This effect is maximized near the critical latitude, where the nearly circular tide forcing the model is at its maximum magnitude of velocity at every phase of the tidal cycle. Above the critical latitude, free internal waves at the M_2 frequency are not permitted, but waves trapped to the feature may exist. In fact, some trapping may occur at high latitudes below the critical latitude as well, so more run time was required to verify that the model reached steady state.

The decreased sensitivity on the RIA is reasonable given that the tidal current now has two components, one parallel and one perpendicular to the ridge. We can view the tide in terms of zonal and meridional components, or components parallel and perpendicular to the ridge, or components along any axis. If we choose the principal components of the tidal ellipse, then the components in the semi-major and semi-minor directions are 90° out of phase, so the net effect of the tide may be thought of as a superposition of two rectilinear tides out of phase by 90°. This 90° phase difference eliminates any interference between the two components, so that the net energy flux is the sum of the energies of the individual principal components of the tide. Motivated by Equation (36) of Llewellyn Smith and Young (2002), we include the dependence of the energy flux on the square of the tidal velocity, and label the principal components of the tidal velocity U_1 and U_2 in order of their magnitude. These components are associated with their own effective widths C_1 and C_2 and complementary RIAs ϕ_1 and ϕ_2. The total energy flux produced is

$$E \propto \frac{U_1^2 H^2 C_1^2}{AB} + \frac{U_2^2 H^2 C_2^2}{AB}. \tag{4.1.1}$$

Since $\phi_2 = 90^\circ - \phi_1$, the total energy flux can be written in terms of the RIA for the major principal component:

$$E \propto \frac{\left(U_1^2 A^2 + U_2^2 B^2\right) H^2 \cos^2 \phi_1}{AB} + \frac{\left(U_1^2 B^2 + U_2^2 A^2\right) H^2 \sin^2 \phi_1}{AB}. \tag{4.1.2}$$

The two resulting coefficients are now closer in magnitude; the ratio of the energy flux at the perpendicular and parallel extremes is not as large with an elliptical tide as it is with a rectilinear tide. Two limiting cases of 4.1.2 are 1) a circular seamount with an elliptical tide, and 2) an elliptical seamount with a circular tide. In the first case of a circular seamount, $A = B = C$, so the total flux is independent of the RIA:

$$E \propto \left(U_1^2 + U_2^2\right) H^2. \tag{4.1.3}$$

The second limiting case has $U_1 = U_2 = U$ for different A and B, so that the tidal velocity is circular but the ridge is elliptical. Again, the total energy flux is independent of the RIA:

$$E \propto \frac{U^2 H^2 \left(A^2 + B^2\right)}{AB}. \tag{4.1.4}$$

This is seen in Figure 4.3; with the forcing wave nearly circular, the total generation is effectively independent of the RIA. The main point remains that the baroclinic energy flux is predictable for an arbitrary RIA, knowing the orientations of the tidal ellipse and the ridge.

Chapter 5

Conclusions

The time-averaged, depth-integrated baroclinic energy flux generated by the barotropic tide flowing at an arbitrary oblique angle over supercritical, idealized three-dimensional undersea ridges is reasonably predictable from an empirical relationship found between the relative incidence angle between the tide and the ridge, and the known solution at a specific angle (e.g., the tide flowing perpendicular or parallel to the long axis of the ridge). The relationship follows by assuming that the generated baroclinic energy flux is proportional to two factors representing the blocking effect and the near-critical slope needed for significant internal tide generation: 1) the area perpendicular to the path of the tide, and 2) the the maximum of the ridge slope when approached from the same direction; i.e. the directional derivative, such as the slopes represented schematically in Figure 2.4.

For a simple rectilinear surface tide, the numerical model used here shows that the energy flux is a maximum when the tide flows perpendicular to the long axis of the ridge and a minimum when the tide flows parallel to the long axis of the ridge. For ridges with elliptical horizontal cross-sections forced by rectilinear tides, a key non-dimensional parameter summarizing the three-dimensional nature of the problem is the quantity C^2/AB from Eqn. 3.4.33, involving the relative incidence angle (RIA) between the tide and ridge and the aspect ratio B/A of the semi-major and semi-minor axes of the ridge. The flux in the perpendicular regime (RIA = 90°) is magnified over that of the parallel regime (RIA = 0°) by the square of B/A. The flux at other angles is a linear combination of these two end cases with the contributions determined by the RIA of the tide to the ridge, and may also be expressed in terms of the flux generated by an infinitely long ridge,

essentially the solution of the two-dimensional problem. For a circularly symmetric seamount or circular surface tidal currents, the dependence on the relative incidence angle vanishes.

Supercritical ridges radiate beams of energy both upwards and downwards that eventually reflect off the surface and seafloor. The azimuth of maximum energy flux is between the surface tidal propagation direction and the line normal to the ridge. The upward-directed beam's larger directivity shows that it is more narrowly focused than the downward-directed beam. The focusing of the upward beam mirrors the focusing of upward paths near the ridge top. Near the top of a slightly supercritical ridge, the topography is convex, allowing more possible paths for energy to radiate away at characteristic slopes, including converging upward paths toward the ridge and over the top and far side. The downward paths from this same critical region near the ridge crest must necessarily diverge, leading to a wider beam of energy that fans out as it propagates away from the ridge, seen in the horizontal cross-sections of Figure 2.3.

When an elliptical barotropic tidal velocity flows over the ridge, more baroclinic energy is produced for the same surface tidal current and the directivity of the upward beams is reduced. An elliptical tidal current may be decomposed into principal components 90° out of phase with each other along the semi-major and semi-minor axes of the tidal ellipse. This makes the net energy flux a linear combination of the individual effects of each principal component, each with their own relative incidence angle to the ridge. When the tide becomes circular, again the angular dependence vanishes; the baroclinic energy flux is independent of the orientation of the ridge.

The empirical relation at the heart of these predictions predicting baroclinic energy flux generation breaks down for ridges perpendicular to the tide as the slope becomes very supercritical ($\epsilon \gtrsim 3$) and even sooner for even slightly supercritical narrow circular pinnacles ($\epsilon \simeq 1.1$). In both cases the method overestimates the baroclinic energy flux that should be produced, probably because approximating the blocking effect by the effective area the ridge or seamount presents to the tide fails to capture how easily the surface tide can simply divert around such steep features. The fact that the circular seamount case diverges from the empirical prediction even sooner than the perpendicular ridge case supports this conjecture. But for topography with more gradual slopes than these limits, the ability to determine the generation at an arbitrarily oriented ridge may allow

for estimates of conversion of barotropic energy to baroclinic by knowing the bottom topography and surface tidal velocities without detailed modeling. When the effects of other parameters, such as the fraction of the water column height filled by the seamount or tidal excursion parameters, are fully investigated, this will help further illuminate the role of internal tides in the transfer and dissipation of total tidal energy.

Bibliography

Baines, P. G. (1973). The generation of internal tides by flat-bump topography. *Deep-Sea Research*, 20:179–205.

Balmforth, N. J. and Peacock, T. (2009). Tidal conversion by supercritical topography. *Journal of Physical Oceanography*, page doi: 10.1175/2009JPO4057.1.

Bell, T. H. (1975a). Lee waves in stratified flows with simple harmonic time dependence. *Journal of Fluid Mechanics*, 67:705–722.

Bell, T. H. (1975b). Topographically generated internal waves in the open ocean. *Journal of Geophysical Research*, 80(3):320–327.

Blumberg, A. F. and Mellor, G. L. (1987). A description of a three-dimensional ocoastal ocean circulation model. In Heaps, N. S., editor, *Three-dimensional coastal ocean models*, Coastal and Estuarine Sciences 4, pages 1–16. American Geophysical Union, Washington, D. C.

Carter, G. S. and Merrifield, M. A. (2007). Open boundary conditions for regional tidal simulations. *Ocean Modelling*, 18:194–209.

Carter, G. S., Merrifield, M. A., Becker, J. M., Katsumata, K., Gregg, M. C., Luther, D. S., Levine, M. D., Boyd, T. J., and Firing, Y. L. (2008). Energetics of M_2 barotropic-to-baroclinic tidal conversion at the Hawaiian Islands. *Journal of Physical Oceanography*, 38(10):2205–2223.

Dushaw, B. D. (2006). Mode-1 internal tides in the western North Atlantic Ocean. *Deep-Sea Research I*, 53:449–473.

Egbert, G. D. and Ray, R. D. (2000). Significant dissipation of tidal energy in the deep ocean inferred from satellite altimeter data. *Nature*, 405:775–778.

Eriksen, C. C. (1982). Observations of internal wave reflection off sloping bottoms. *Journal of Geophysical Research*, 87(C1):525–538.

Ezer, T. and Mellor, G. L. (1997). Simulations of the Atlantic Ocean with a free surface sigma coordinate ocean model. *Journal of Geophysical Research*, 102(C7):15,647–15,657.

Flather, R. A. (1976). A tidal model of the north-west European continental shelf. *Memoires de la Societe Royale des Sciences de Liege*, 6(10):141–164.

Garrett, C. and Kunze, E. (2007). Internal tide generation in the deep ocean. *Annual Review of Fluid Mechanics*, 39:57–87.

Gill, A. E. (1982). *Atmosphere-Ocean Dynamics*, volume 30. Academic Press.

Hall, R. A. and Carter, G. S. (2010). Internal tides in monterey submarine canyon. *Journal of Physical Oceanography*, 41.

Haney, R. L. (1991). On the pressure gradient force over steep topography in sigma coordinate ocean models. *Journal of Physical Oceanography*, 21:610–619.

Holloway, P. E. and Merrifield, M. A. (1999). Internal tide generation by seamounts, ridges, and islands. *Journal of Geophysical Research*, 104(C11):25,937–25,951.

Kantha, L. H. (1995). Barotropic tides in the global oceans from a nonlinear tidal model assimilating altimetric tides 1. model description and results. *Journal of Geophysical Research*, 100(C12):25,283–25,308.

Kunze, E., Rosenfeld, L. K., Carter, G. S., and Gregg, M. C. (2002). Internal waves in Monterey Submarine Canyon. *Journal of Physical Oceanography*, 32:1890–1913.

Llewellyn Smith, S. G. and Young, W. R. (2002). Conversion of the barotropic tide. *Journal of Physical Oceanography*, 32:1554–1566.

Llewellyn Smith, S. G. and Young, W. R. (2003). Tidal conversion at a very steep ridge. *Journal of Fluid Mechanics*, 495:175–191.

Medwin, H. and Blue, J. E. (2005). *Sounds in the sea: From ocean acoustics to acoustical oceanography*. Cambridge University Press.

Mellor, G. L., Ezer, T., and Oey, L.-Y. (1994). The pressure gradient conundrum of sigma coordinate ocean models. *Journal of Atmospheric and Oceanic Technology*, 11(8):1126–1134.

Mellor, G. L. and Yamada, T. (1982). Development of a turbulence closure model for geophysical fluid problems. *Reviews of geophysics and space physics*, 20(4):851–875.

Merrifield, M. A. and Holloway, P. E. (2002). Model estimates of M_2 internal tide energetics at the Hawaiian Ridge. *Journal of Geophysical Research*, 107(C8):10.1029/2001JC000996.

Munroe, J. R. and Lamb, K. G. (2005). Topographic amplitude dependence of internal wave generation by tidal forcing over idealized three-dimensional topography. *Journal of Geophysical Research*, 110.

Niwa, Y. and Hibiya, T. (2001). Numerical study of the spatial distribution of the M_2 internal tide in the Pacific Ocean. *Journal of Geophysical Research*, 106(C10):22,441–22,449.

Rainville, L. and Pinkel, R. (2006). Baroclinic energy flux at the Hawaiian Ridge: Observations from the R/P FLIP. *Journal of Physical Oceanography*, 36(6):1104–1122.

Simmons, H. L., Hallberg, R. W., and Arbic, B. K. (2004). Internal wave generation in a global baroclinic tide model. *Deep-Sea Research II*, 51(25–26):3043–3068.

St. Laurent, L., Stringer, S., Garrett, C., and Perrault-Joncas, D. (2003). The generation of internal tides at abrupt topography. *Deep-Sea Research I*, 50:987–1003.